Homogenization Mechanism of Spinodally Decomposed Polymer Blends via Baker's Transformation

Alexander E. Ribbe and Takeji Hashimoto*

Hashimoto Polymer Phasing Project, ERATO, JST, and Department of Polymer Chemistry, Graduate School of Engineering, Kyoto University, Kyoto 606-8501, Japan

Received May 1, 2000; Revised Manuscript Received July 25, 2000

ABSTRACT: An uniaxial compression process is repeatedly applied at room temperature to homogenize an immiscible polymer blend composed of a random copolymer of poly(styrene-*ran*-butadiene) and polybutadiene. The different stages of this process are investigated by transmission electron microscopy, laser scanning confocal microscopy, and light scattering. The bicontinuous phase-separated morphology developed in the as-prepared sample is transformed into a lamellar-like morphology with the lamellar normals preferentially oriented parallel to the compression axis upon applying this process. The characteristic spacing parallel to the compression axis is decreasing constantly, and when the spacing becomes smaller than the critical length, the homogenization finally occurs.

I. Introduction

The structure formation of polymer blends during the process of phase separation via spinodal decomposition (SD) is a widely discussed phenomenon in the field of polymer physics. We have been studying the time dependence of scattering patterns during SD from mixtures such as poly(vinylmethyl ether)/polystyrene,[1−4] polyisoprene(PI)/polybutadiene (PB),[5−7] or polybutadiene/poly(styrene-*ran*-butadiene) (SBR)[8−12] which undergo sufficiently slow phase separation, to explore the time evolution of the structural change in reciprocal space. Mixtures of PI and PB having LCST were intensively studied by scattering techniques,[5−7] and a direct observation of the morphological change during SD of this system by light microscopy has been presented.[13,14]

The here discussed mixture of PB and SBR has an UCST type phase diagram with a rather high critical temperature of about 170 °C[15] or even higher.[8,16] Forcing such a system into a single-phase state simply by raising the temperature is not possible, as the cloud point is far above the degradation temperature of the two polymers. For such mixtures a mechanical folding−pressing process known as "Baker's transformation" can be applied.[16,17] This folding−pressing procedure, which involves folding of an as-prepared film containing phase-separated structure and then pressing it manually between two glass plates with spacers of its original thickness, as schematically shown in Figure 1, has been successfully applied to obtain homogeneous mixtures of a SBR/PB blend for the investigation of spinodal decomposition by light scattering and light microscopic[8−12] and electron microscopic methods.

The following process was proposed on the homogenization by Baker's transformation[16] which involves a repeated uniaxial compression. The characteristic domain spacing $\Lambda_{||}$ parallel to the direction of the applied uniaxial compression decreases very rapidly, while the characteristic spacing $\Lambda_{\perp}$ perpendicular to the compression axis slowly increases. As described in detail in a previous paper,[16] the decrease of $\Lambda_{||}$ and the increase of $\Lambda_{\perp}$ can be roughly described by a simple affine deformation which is schematically given in Figure 2: The changes of $\Lambda_{||}$ and $\Lambda_{\perp}$ are given by

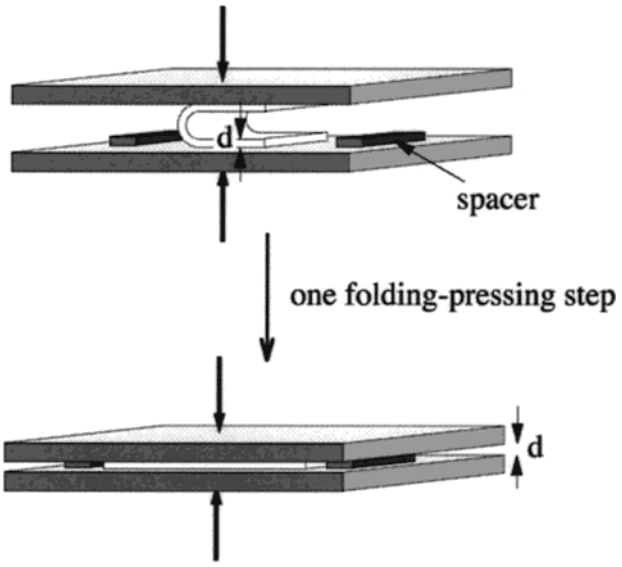

Figure 1. Illustration of the folding−pressing process, the so-called "Baker's transformation", applied in order to transform the phase-separated polymer blend into the homogeneous state.

$$\Lambda_{||} = \Lambda_0(1/2)^n \tag{1a}$$

and

$$\Lambda_{\perp} = \Lambda_0 2^{n/2} \tag{1b}$$

where n is the number of applied folding−pressing steps and Λ_0 the initial domain spacing of the as-prepared sample. Accordingly, $\Lambda_{||}$ is decreasing very rapidly and reaches 10 Å after only $n = 10$ folding−pressing steps with an initial Λ_0 of 1 μm, while $\Lambda_{\perp}$ is increasing by a factor of 32. This situation is thermodynamically very unstable as the gradient of the free energy parallel to the compression axis becomes very high and $\Lambda_{||}$ becomes smaller than the critical length as predicted by the Cahn−Hilliard theory;[18] therefore, the remaining struc-

10.1021/ma000752d CCC: $19.00
Published on Web 09/21/2000

Table 1. Characteristics of Polybutadiene (PB20) and Poly(styrene-*ran*-butadiene) (SBR20) Polymers Used in This Study

	styrene content[a] (wt %)	N_W[b]	M_W[b]	M_W/M_N[b]	microstructure of butadiene unit[a] (%)		
					1,4-cis	1,4-trans	1,2-vinyl
polybutadiene (PB20)		4.13×10^3	2.23×10^5	1.3	23	37	40
poly(styrene-*ran*-butadiene) (SBR20)	20	3.00×10^3	1.79×10^5	1.2	17	31	52

[a] Determined by NMR. [b] Determined by GPC.

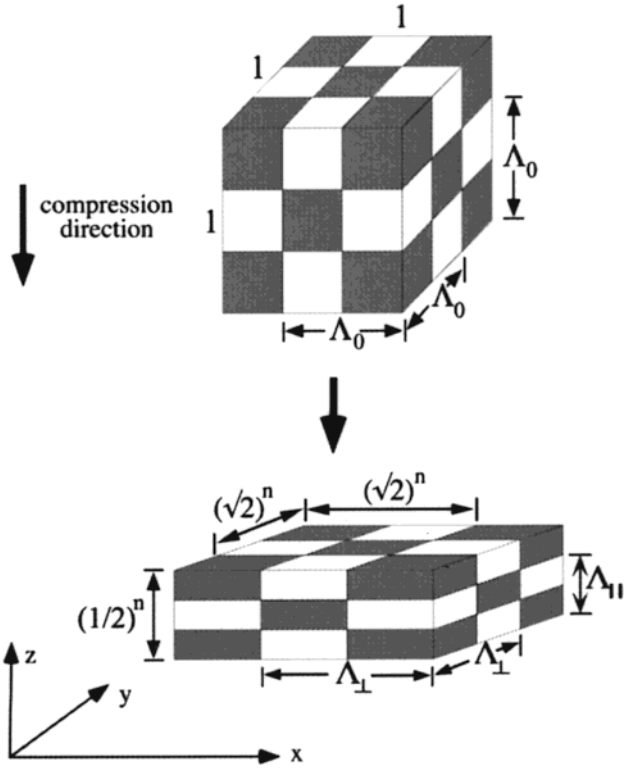

Figure 2. Schematic illustration of the affine deformation model for the change of the domain spacing parallel and perpendicular to the compression direction during the Baker's transformation process.

ture should be dissolved into a homogeneous (or single phase) mixture.

Here we present a detailed morphological investigation of the folding−pressing process, especially by TEM and laser scanning confocal microscopy (LSCM) methods, in order to verify the proposed mechanism. By staining with OsO_4, which allows a selective staining and cross-linking[15,19] of the butadiene sequence of SBR and PB and therefore pinning of further growth of the phase-separated domains, the structural change during the folding−pressing process is visualized.[15] For lower resolution laser scanning confocal microscopy, which has become a helpful tool in the investigation of multiphase polymer systems,[20−22] was applied and discussed in comparison with the TEM images.

II. Experimental Part

II.A. Sample. The two polymers coded as SBR20 and PB20 have molecular weight and microstructure given in Table 1. The binary mixture used in this experiments has a near critical composition of 47 vol % SBR (50/50 wt %/wt % SBR/PB). The polymers were dissolved in toluene, containing 5 wt % polymer in total. This solution was cast into thin film specimens in Petri dishes, where the solvent was allowed to evaporate over 1 week at 30 °C. The 0.15 mm thick samples were further dried in a high-vacuum oven until no mass loss could be observed.

II.B. Mechanical Mixing. As mentioned above, the two-phase morphology of the as-cast film cannot be transformed to a single-phase state by raising the temperature. Therefore, a previously described mechanical mixing process called Baker's transformation[17] was applied at room temperature. As depicted in Figure 1, the film is folded and pressed between two glass plates until the original thickness is regained. This process was repeated for several times until the mixture became homogeneous. Since the homogenized state is thermodynamically unstable, immediately after the homogenization phase separation starts.

II.C. Transmission Electron Microscopy. The samples obtained after the respective folding−pressing steps were cooled in ice water and then in liquid nitrogen. The thus obtained samples were then cut into ultrathin sections using a low-temperature ultramicrotome Reichert/Nissei Ultracut FC4E equipped with a diamond knife at −100 °C, and the 30−50 nm ultrathin sections were stained with OsO_4 vapor, while warming the sections to room temperature. We used high molecular weight polymers for this examinations in order to have a sufficiently slow phase separation. This is to avoid artifacts induced by a further growth of the phase-separating structure during the staining process of the sample as much as possible. A staining for 1−2 min was sufficient enough to obtain good contrast in the TEM. As a helpful side effect, the staining procedure cross-links the PB phase[15] and therefore terminates any further phase separation. A TEM (Hitachi HS600) with 100 kV acceleration voltage was used. The TEM negatives were digitized using a high-resolution scanner, and 512 × 512 pixel sized areas were used to perform 2D Fourier transformations using the TEM supplied firm software, "Digital Micrograph (Gatan)". The circular averaging was done by using a small self-written C program. Details regarding the subsequent data analysis were already described elsewhere.[15]

II.D. Laser Scanning Confocal Microscopy. No special treatment of the sample was required for laser scanning confocal microscopy (LSCM). LSCM measurements were done with a LSM 320 (ZEISS) using a He/Ne laser with $\lambda = 632.8$ nm wavelength, and image processing was done with the firm software supplied by Zeiss. The microscope has an excellent spatial resolution along the depth direction because of the following mechanism. The laser beam from the light source is passed through a beam splitter and focused on the sample via the scanner through the tube lens and objective lens. Light reflected or emitted from the focal plane is directed back through the objective lens, the tube lens, the scanner, and the beam splitter. It is then focused on and passed through a pinhole and directed to the detector. The light emanating from other planes cannot pass through the pinhole as it is focused at places other than the pinhole position and hence is effectively suppressed. A photomultiplier is used as detector. A detailed description of the apparatus[23] and the image generation[24−30] can be found in the literature. The contrast between the two phases is generated by reflected light[23] at the interface of the two phases and by excess scattering arising from the SBR phase in the SBR/PB mixture (scattering-induced contrast generation)[24,26]

II.E. Light Scattering. The time-resolved light scattering (TRLS) was carried out with a laser with $\lambda = 632.8$ nm wavelength. A detailed description of the apparatus is given elsewhere.[1]

III. Results and Discussion

III.A. Light Scattering. Figure 3 shows a scheme of the observation directions utilized by the different methods. While the LS and LSCM techniques allow an

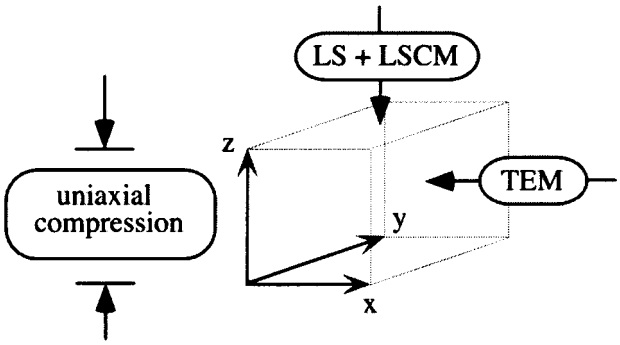

Figure 3. Scheme showing the observation directions of the TEM, LSCM, and LS methods used in this study.

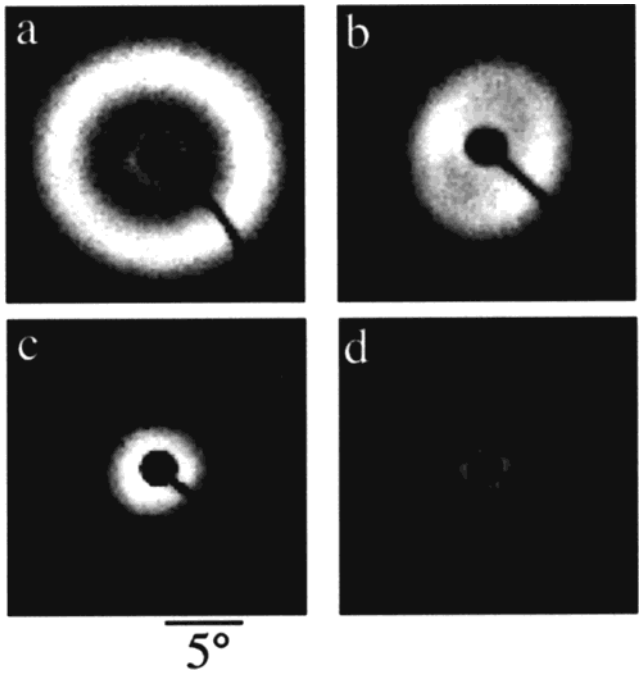

Figure 4. Light scattering patterns obtained with incident beam parallel to the compression axis of the as-cast sample (a), after the first folding−pressing (b), after the fourth folding-pressing (c), and after the 15th folding−pressing (d).

observation along the axis of the uniaxial compression (*z*-axis), the observation direction of the TEM is perpendicular to it.

The scattering pattern of the as-cast sample depicted in Figure 4a shows a spinodal ring due to the phase-separated morphology developed during the solvent evaporation process. A maximum scattered intensity I_m can be observed at magnitude of scattering vector q equal to a particular wavenumber of $q_{m,0} = 6.7 \times 10^{-4}$ nm^{-1}, from which a domain spacing of $\Lambda_{m,0} = 2\pi/q_{m,0} =$ 9.4 μm can be evaluated.

The scattering vector at maximum scattered intensity caused by the composition fluctuations in the *x*,*y*-plane (Figure 3) after the *n*th folding−pressing step is defined hereafter as $q^{LS}_{m,\perp}(n)$. This value after the first folding−pressing step decreases to $q^{LS}_{m,\perp}(n=1) = 4.8 \times 10^{-4}$ nm^{-1} (see Figure 4b), which is equal to an increase of the average domain spacing of $\Lambda^{LS}_{m,\perp}(n=1) = 13.1$ μm. According to our model shown in Figure 2 and eq 1b, $\Lambda^{theory}_{m,\perp}(n=1)$ should be equal to $(2)^{1/2}\Lambda_{m,0} = 13.3$ μm. This value is in good agreement with the experimentally determined value $\Lambda^{LS}_{m,\perp}(n=1) = 13.1$ μm, showing that the model is working quite well.

For the following folding−pressing steps, the localization of the peak maximum becomes rather difficult, as it is moving very close to the beam stop for the incident beam as seen after the fourth (Figure 4c) and 15th folding step (Figure 4d). The increase of the characteristic domain spacing $\Lambda^{LS}_{m,\perp}$ observed in the *x*,*y*-plane causes the peak maximum to vanish under the beam stop. Accompanied by the peak shift, the peak intensity tends to decrease. After the 30th folding−pressing step, no scattered intensity can be detected at all (not depicted). This indicates that, as the domain spacing expands normal to the compression axis far above the resolution limit of our scattering setup, the phase-separated structures are progressively homogenized toward a single phase state.[16]

III.B. Transmission Electron Microscopy. The structural evolution of the single stages during the folding−pressing procedure is illustrated by their TEM micrographs shown in Figure 5a−e.

The as-cast sample (Figure 5a) shows a periodic bicontinuous phase-separated structure, which has recently been characterized as a spongelike structure,[26−30] with an average domain spacing of $\Lambda^{TEM}_{||}(n=0) = 8.6$ μm as calculated from the 2D-FFT spectrum (see later in text; Figure 6 and Table 2).[15,24] The dark areas correspond to PB-rich domains stained by OsO_4, while the bright areas correspond to less stained SBR-rich domains. For $n = 0$, i.e. as-prepared sample, the bicontinuous phase-separated structure shows the same periodic spacing in three dimensions, and therefore $\Lambda_{||}(n=0)$ is equal to $\Lambda_{\perp}(n=0)$ and directly comparable to the light scattering data. The average domain spacing determined by LS was $\Lambda^{LS}_{m,0}(n=0) = 9.4$ μm and is in reasonably good agreement with $\Lambda^{TEM}_{||}(n=0) = 8.6$ μm obtained from the TEM-FFT measurement, considering that the TEM image is covering a only small sample area compared to the light scattering method. The domain spacing is very large compared to the sections thickness—about 50 nm—of the ultrathin slice used for TEM; therefore, only a very limited area is depicted. To get a better 3-dimensional view of a structure with comparably large domain spacing, the LSCM is a better tool, which will be shown in the next section (III.C).

The TEM image in *y*,*z*-plane after the first folding−pressing step is given in Figure 5b. The structures clearly show an elongation in horizontal direction of the image, which suggests that the applied compression axis is nearly vertical for the here selected image. The interconnected structure is strongly deformed, and some of the interconnections break up due to the applied deformation as seen by the portion marked by a large white arrow. The intensity maximum of this structure parallel to the compression axis should move to higher q range, and therefore the structure parallel to the compression axis should have a smaller domain spacing. The direct observation of the scattering pattern in this plane, however, is very difficult. We can obtain information about the average domain spacing in this direction from the 2D-FFT pattern of the TEM image. We shall discuss the structure marked with small arrows and encircled by a white line in conjunction with the LSCM image given in Figure 7c and Figure 8 later in the text.

In the case of an isotropic scattering pattern, like in the case of the as-prepared sample $n = 0$ (Figure 4a), we can circularly average the Fourier spectrum and obtain the characteristic wavelength from the wavenumber at intensity maximum. Curve a of Figure 6

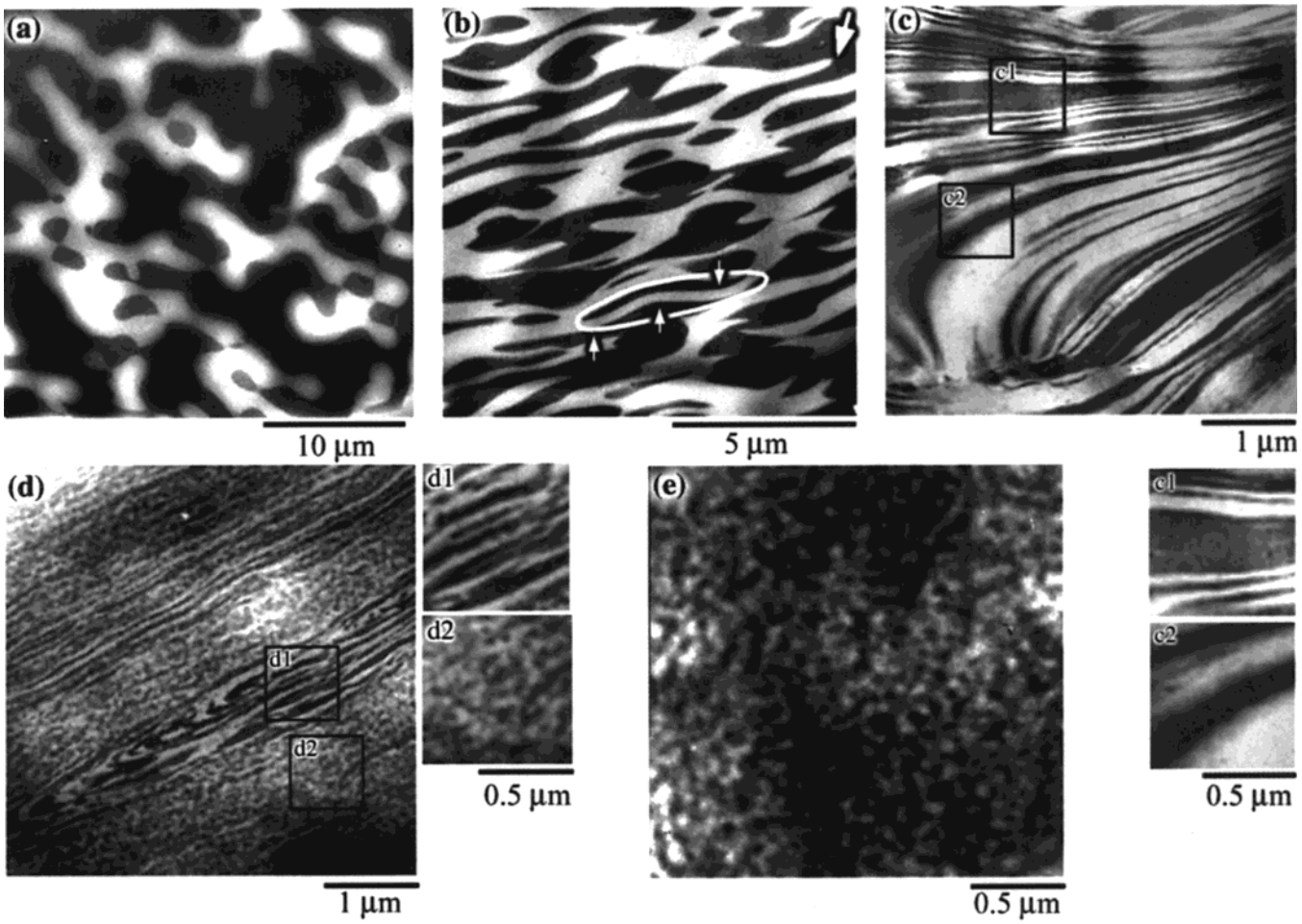

Figure 5. TEM micrographs obtained for the as-cast sample (a) and for the specimens after the first folding−pressing (b), after the fourth folding-pressing (c), after the 15th folding−pressing (d), and after the 30th folding−pressing step (e). The micrographs show images observed for ultrathin sections cut parallel to *y*,*z*-plane in Figure 3.

Table 2. Average Domain Spacing $\Lambda_{||}$, $\Lambda_{\perp}$ and Corresponding Wavenumber $q_{m,||}$, $q_{m,\perp}$ Observed Parallel or Perpendicular to the Direction of the Compression Axis Determined by 2-D Fourier Transformation of the TEM Images (TEM_{FFT}) and by Light Scattering (LS) Experiments and Theoretical Values Derived from the Model Given in Figure 2

	$\Lambda_{||}$ [μm]		$q_{m,||}$ [nm^{-1}]		$\Lambda_{\perp}$ [μm]		$q_{m,\perp}$ [nm^{-1}]	
n	TEM_{FFT}	theor	TEM_{FFT}	theor	LS	theor	LS	theor
0	8.6		7.3×10^{-4}		9.4		6.7×10^{-4}	
1	4.0	4.3	1.6×10^{-3}	1.3×10^{-3}	13.1	13.3	4.8×10^{-4}	4.8×10^{-4}
4	0.28	0.54	2.2×10^{-2}	1.1×10^{-2}				
15	0.17	(2.6×10^{-4})	3.7×10^{-2}					
30[a]	0.078	(8.8×10^{-6})	8.1×10^{-2}					

[a] From Ribbe and Hashimoto.[15]

shows the circularly averaged spectrum of the as-prepared sample and determines $\Lambda_{||}^{TEM}(n=0) = 8.6\ \mu$m. In the case of an anisotropic pattern we use sector averaging with a width of ±10° in direction of the peak maxima caused by the lamella-like structures whose normals are parallel to the compression axis. The resulting spectra are given in Figure 6, curves b−d. The spectrum for the homogenized sample was already given elsewhere.[15] From curve b of Figure 6 we determine the average domain spacing after the first compression step to $\Lambda_{||}^{TEM}(n=1) = 4.0\ \mu$m. From our model described by eq 1a we calculate $\Lambda_{||}^{theor}(n=1) = 4.3\ \mu$m, which is again in good agreement with the experimentally determined value.

As seen in Figure 5c, the deformation observed in the *z*-direction appears to be larger than that expected for the affine deformation after the fourth folding−pressing step. The TEM image shows a fine lamella-like structure with smallest domain spacing of about 200 nm. Because of shearing effects during the folding−pressing process and orientation distribution of the domains before compression, the lamellar normals are not necessarily preferentially oriented parallel to the compression axis. Grains of lamellae with different orientation are visible. The average domain spacing obtained from the 2D-FFT analysis ($\Lambda_{||}^{TEM}(n=4) = 280$ nm) is about 2 times smaller than the theoretical value ($\Lambda_{m,||}^{theory}(n=4) = 540$ nm). The following explanations for this discrepancy seem reasonable: (i) as mentioned above, only a limited area can be observed by the TEM; (ii) the folding−pressing procedure depends strongly on the operator, meaning that each folding−pressing step will not be applied in exactly the same manner, and sharing effects will play an important role in the structure formation; (iii)

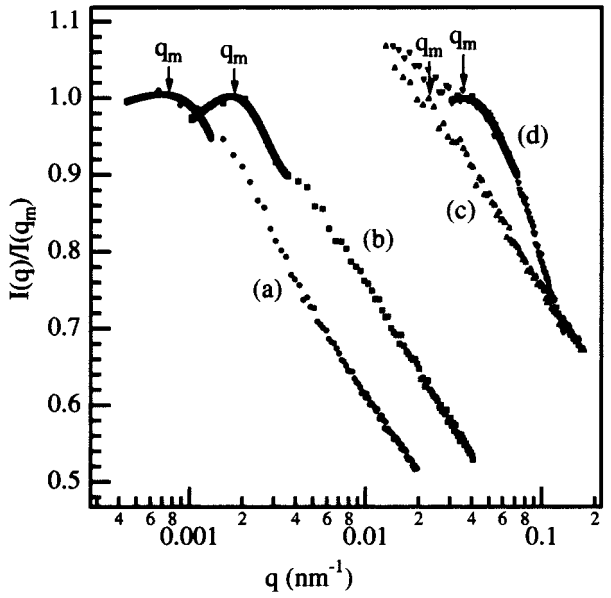

Figure 6. Circular (a) and sector-averaged profiles (b−d) of the 2D-FFT spectra $I(q)/I(q_m)$ obtained from the TEM images depicted in Figure 5; q is the scattering vector, and q_m is the q value at maximum intensity. (a) For as-cast, (b) after the first folding−pressing step, (c) after the fourth folding−pressing step, and (d) after the 15th folding−pressing step. Spectra b−d correspond to those parallel to the compression axis.

deformation becomes progressively heterogeneous and nonaffine. Looking carefully at the details of the image, one can see that there are already areas, exemplary enlarged in parts (inset c1) and (inset c2), where the lamellar spacing is already so small that the lamellae tend to dissolve into a homogenized state, showing a contrast similar to that observed for the homogeneous state in part e as will be described in the next paragraphs. This indicates that the homogenization process already starts locally at this early stage of the folding−pressing procedure.

As visible from the TEM image in Figure 5d, the domain spacing again decreases dramatically after the 15th folding−pressing step. Besides areas that still show a lamella-like morphology (inset d1), there are regions that show a morphology (inset d2) very reminiscent of the frozen thermal composition fluctuations in the disordered state in block copolymers reported by Hashimoto and co-workers.[31−33] The contrast observed in inset d2 in Figure 5d is identical to the contrast of the image of the homogenized state depicted in Figure 5e discussed later in the text. Therefore, in those regions the lamella morphology broke up to form a homogeneous mixture with composition fluctuations. Under the TEM it is difficult to distinguish between diffuse and sharp interfaces, and whether we still observe contrast caused by a real phase-separated structure or only contrast caused by frozen thermal composition fluctuations. Our previous studies support the latter case.[15] According to our model, the average domain spacing after the 15th folding−pressing step is much smaller than the critical length $\Lambda_c = 2\pi/q_c$ ($\approx$70 nm[15]), where q_c is the critical wavenumber above which the q-dependent growth rate becomes negative in the Cahn−Hilliard theory;[18] hence, the mixture should be homogeneous at this stage (see Table 2). The average characteristic domain spacing determined by 2D-FFT is $\Lambda_{||}^{TEM}(n=15) = 170$ nm. During the folding−pressing process, the mixing induced by the folding−pressing process is always in competition with the onset of the demixing process due to SD, which starts immediately after the cessation of the compression. The observed structure in the inset d2 of Figure 5d might therefore be caused by the bicontinuous morphology developed during the very early stage of the SD or by the frozen disordered state close to the critical point.[15]

The TEM image after the 30th folding step, which represents the homogenized state, is given in Figure 5e. We observe a fine structure which is caused by either frozen thermal composition fluctuations or the very early stage of phase separation after the mixing procedure. In either case the observed contrast is caused by PB-rich and PB-poor domains, which are responsible respectively for the dark and bright contrast under the TEM due to the above-described preferential staining by OsO_4. The characteristic spacing ($\Lambda_{||}^{TEM}(n=30)$) was determined to be 78 nm. An interpretation of this result was discussed in a previous paper.[15]

III.C. Laser Scanning Confocal Microscopy. Parts a−d of Figure 7 are the LSCM images at the different stages of the folding−pressing procedure corresponding to the TEM images given in Figure 5a−d. The LSCM images were obtained by recording a series of 15 consecutive sliced images along the z-direction, each image having a focal depth of 750 nm and a distance of 500 nm apart from each other. The 15 sliced images stacked on top of each other in order to construct the three-dimensional (3D) images. In each image in Figure 7a−d, part A shows an image for the top slice of the series, and parts B and C are cross-sectional images parallel to y,z- and x,z-planes along the white lines in part A, respectively. The line marked by "as" in parts B and C in each image a to d gives the location of the polymer/air interface in each image. As described in previous works,[15,21,26,27] the contrast of an LSCM image obtained in reflection mode is mainly caused by the reflected light at the interface between the two polymers, where a change in the refractive index takes place. As the reflection of the laser light by an interface perpendicular to the beam direction will cause greatest intensity, the brightest areas correspond to maximum reflection, which is caused by a structure unit whose interfaces are normal to the incident beam. In the case of the as-cast sample depicted in Figure 7a, one of those areas is marked by a white arrow in part A. Besides the contrast generated by reflection at interfaces, the SBR phase itself shows a slightly higher contrast compared to the PB phase, which might be caused by scattering due to local composition fluctuations or a microheterogeneous structure caused by the styrene and butadiene units in the SBR-rich phase ("scattering-induced contrast generation").[24]

Figure 8 shows a model illustrating the deformation of a spongelike morphology due to the first folding−pressing step. The original morphology given in part a has equal average domain spacing parallel $\Lambda_{||}$ and $\Lambda_{\perp}$ perpendicular to the compression axis. After the first folding−pressing step illustrated in part b, $\Lambda_{||}$ decreases while $\Lambda_{\perp}$ is increasing. The encircled area marks in Figure 8b a place where an undulating tube is formed which is responsible for the string-droplet pattern, whose contrast generation in the LSCM is illustrated in part c of Figure 8 and described later in the text.

Figure 7b shows the LSCM image after the first folding−pressing step corresponding to the TEM image

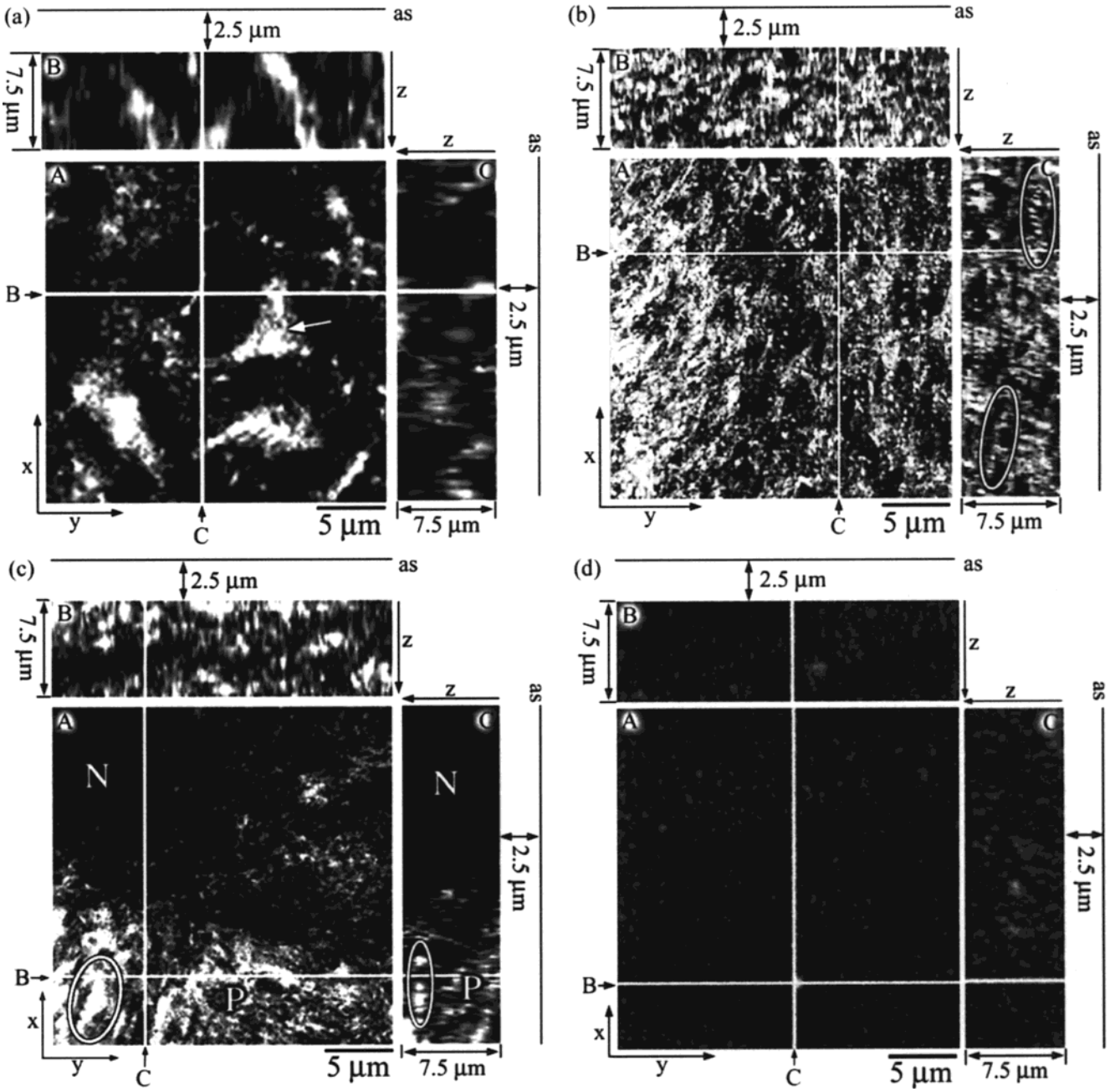

Figure 7. 3D reconstruction of the morphological change during the folding−pressing procedure obtained by LSCM in reflection mode. (a) As-cast sample, (b) after the first folding−pressing step, (c) after the fourth folding−pressing step, and (d) after the 15th folding−pressing step corresponding to the TEM images given in Figure 5a−d, respectively. In all cases a series of 15 consecutive slices of LSCM image with a focal depth of 750 nm and a distance of 500 nm apart from each other was used. Parts A are the top slices of the respective series of the sliced images, and parts B and C are cuts parallel to the *z*,*y*- and *z*,*x*-planes along the white lines B and C in part A, respectively.

which was given in Figure 5b. Because of the applied force, interconnecting tubes (a part of spongelike structures) break up to form sharp edges. One of those is marked by a large white arrow on the TEM image in Figure 5b and is illustrated in the model given in Figure 8c as well. Those edges are partially responsible for the specklelike contrast in the LSCM image. The reflection observed from such an edge is principally the same as that observed for small droplets for which only the top of the sharp edge reflects light toward the detector and therefore appears as a bright spot on the LSCM image. For the artificial elongation of the bright spots in *z*-direction as seen in parts B and C in Figure 7b, the interpretation formulated for droplet morphologies is applicable.[26] Further the compression causes the interface to expand and elongate in direction parallel to the *x*,*y*-plane, which results in an increase of undulating lamellar interface aligned in parallel direction to the *x*,*y*-plane causing a droplet-string pattern; some of those are encircled by a white line in part C of Figure 7b. The contrast of such a droplet-string pattern can be understood from the model in Figure 8c. Because of the compression, a large portion of the interface is aligned with its interface parallel to the compression direction, creating lamellar-like structures with an undulating surface. An undulating lamella creates places where the interface is almost perpendicularly oriented to the incident beam and showing therefore highest intensity. Between the intensity maxima the angular variation of the interface normal causes a decrease of the reflected

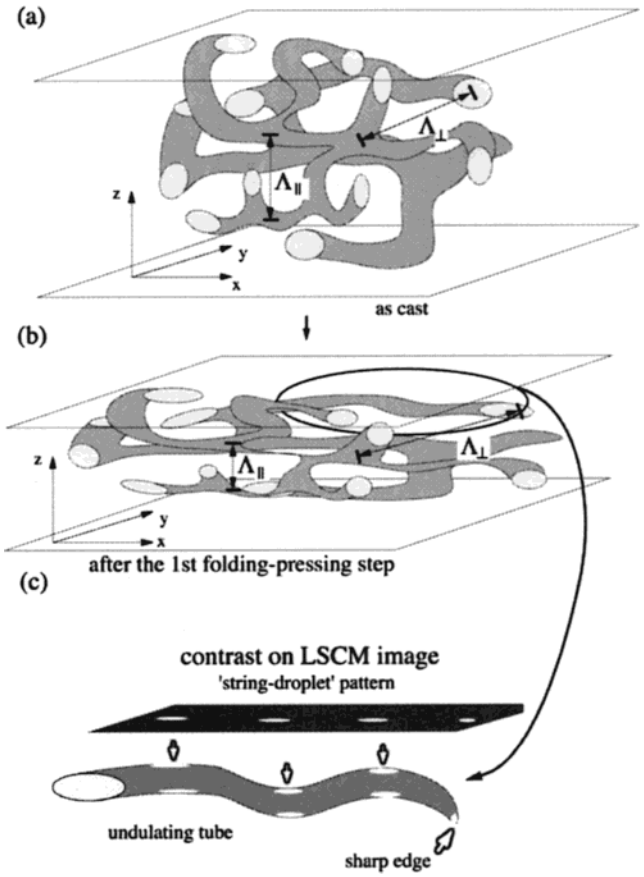

Figure 8. Schematic illustration of the first folding−pressing step (parts a and b) and the interpretation of the string-droplet pattern observed in the LSCM (part c). Schematic representation of the spongelike phase-separated structure in (a) as-cast and before the first folding−pressing step and (b) after the first folding−pressing step.

intensity, leading to the droplet-string pattern. This undulation is also clearly visible on the TEM image which was given in Figure 5b. Exemplarily, one undulating unit is encircled by a white line, and the locations where one expects highest intensity in the LSCM image in Figure 7b are marked by small white arrows in Figure 5b. The distance between all these virtual arrows is in the same range (0.5−2 μm), which corresponds to the distance of the white spots of the string-droplet pattern observed on the LSCM images. The increase of the high-intensity areas in Figure 7b in comparison to the as-cast sample in Figure 7a is related to a transformation of the spongelike structures into lamellar structure with interface oriented parallel to the *x*,*y*-plane due to the folding−pressing procedure, which is directly conceivable from our model in Figure 2. The orientation of the deformed lamellar type interface parallel to the *x*,*y*-plane is directly visible from the orientation of the string-droplet pattern marked exemplarily by white circles in part C of Figure 7b.

The domain spacing of the structures becomes very small after the fourth folding step, as visible on the TEM image seen in Figure 5c, so that the local resolution of the LSCM is too low to resolve single lamellae (see Figure 7c). Nevertheless, the LSCM image gives us a general information about the grain size or their orientation. In Figure 7c, single grains appear with high or low contrast due to their orientation to the incident beam. As illustrated schematically in Figure 9, lamellae with their normals nearly parallel (P-grain in Figure 9) to the incident beam will show a strong reflection and therefore appear bright on the LSCM slice, as all the interfaces of a series of lamella within the focal range (ΔF) contribute to the observed intensity. Such areas are encircled in parts A and C of Figure 7c. The area marked by P shows compared to the area marked by N higher overall intensity, which reflects the N-grain with their lamellar normals inclined with respect to the *z*-axis in Figure 9. The interface of lamella grains with their lamellar normals strongly inclined with respect to the *z*-axis (N-grain in Figure 9) will only reflect a limited ratio of the incident beam in direction to the detector and the observed intensity will therefore be low. Those areas are marked by a symbol N in Figure 7c, parts A and C. Further partially homogenized areas might be causing dark contrast as well.

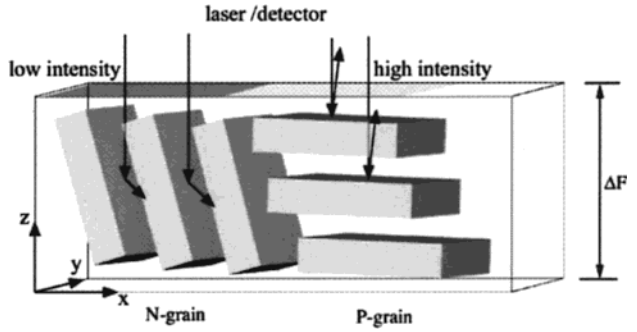

Figure 9. Schematic illustration of the contrast in the LSCM caused by lamella grains with different orientation (N-grain and P-grain in Figure 7c).

After the 15th folding−pressing step no contrast is observed on the LSCM image as seen in Figure 7d. This is due to the fact that the structures are more or less homogenized, and their size becomes smaller than the lateral resolution limit of the microscope of about 250 nm. This is consistent with the TEM observations (Figure 5d) where we found an average domain spacing of 170 nm. For the same reason we obtain the same result in the LSCM after the 30th folding−pressing step, though the image is not shown here.

IV. Summary

We presented a real-space analysis of the structural change of a mechanical folding−pressing process called "Bakers' transformation" of an immiscible polymer blend system of SBR and PB. It could be shown that the original bicontinuous spongelike structure, as observed in the as-cast sample, is transformed via a lamella-like structure into the homogeneous state. The method is an alternative way to obtain a homogeneous mixture in the case T_c of the system is too high, preventing a homogenization by simply annealing at elevated temperatures.

Acknowledgment. The authors thank the Japan Society for Promotion of Science (JSPS), the Alexander von Humboldt Foundation, the European Commission (STF), and the Ministry of Education, Science and Culture and Sports, Japan (Grant-in-Aid for Scientific Research on Priority Areas "Cooperative Phenomena in Complex Liquids" Nr. 07651106), for financial support.

References and Notes

(1) Hashimoto, T.; Kumaki, J.; Kawai, H. *Macromolecules* **1983**, *16*, 641.
(2) Kumaki, J.; Hashimoto, T. *Macromolecules* **1986**, *19*, 764.

(3) Hashimoto, T.; Itakura, M.; Hasegawa, H. *J. Chem. Phys.* **1986**, *85*, 6118.
(4) Hashimoto, T.; Itakura, M.; Shimidzu, N. *J. Chem. Phys.* **1986**, *85*, 6673.
(5) Jinnai, H.; Hasegawa, H.; Hashimoto, T.; Han, C. C. *Macromolecules* **1991**, *24*, 282.
(6) Hashimoto, T.; Takenaka, M.; Jinnai, H. *J. Appl. Crystallogr.* **1991**, *24*, 457.
(7) .Takenaka, M.; Hashimoto, T. *J. Chem. Phys.* **1991**, *96*, 6177.
(8) Izumitani, T.; Hashimoto, T. *J. Chem. Phys.* **1985**, *83*, 3694.
(9) Takenaka, M.; Izumitani, T.; Hashimoto, T. *Macromolecules* **1987**, *20*, 2257.
(10) Izumitani, T.; Takenaka, M.; Hashimoto, T. *J. Chem. Phys.* **1989**, *95*, 3213.
(11) Takenaka, M.; Izumitani, T.; Hashimoto, T. *J. Chem. Phys.* **1990**, *92*, 4566.
(12) Hashimoto, T.; Takenaka, M.; Izumitani, T. *J. Chem. Phys.* **1992**, *97*, 679.
(13) Laeuger, J.; Lay, R.; Maas, S.; Gronski, W. *Macromolecules* **1995**, *28*, 7010.
(14) Laeuger, J.; Lay, R.; Gronski, W. *J. Phys. Chem., Lett.* **1994**, *78*, 1018.
(15) Ribbe, A. E.; Hashimoto, T. *Macromolecules* **1997**, *30*, 3999.
(16) Hashimoto, T.; Izumitani, T.; Takenaka, M. *Macromolecules* **1989**, *22*, 2293.
(17) The term "Baker's transformation" was suggested to T.H. by Dr. E. DiMarzio (NIST, Gaithersburg, MD) and first used in the literature by: Hashimoto, T.; Izumitani, T. *Macromolecules* **1993**, *26*, 3631.
(18) Cahn, J. W.; Hilliard, J. E. *J. Chem. Phys.* **1959**, *31*, 688. Cahn, J. W. *J. Chem. Phys.* **1965**, *42*, 93.
(19) Ribbe, A. E.; Bodycomb, J.; Hashimoto, T. *Macromolecules* **1999**, *32*, 3154.
(20) Verhoogt, H.; van Dam, J.; Posthuma de Boer, A.; Houpt, P. M. *Polymer* **1993**, *34*, 1325.
(21) Li, L.; Sosnoowski, S.; Chaffey, C. E.; Balke, S. T.; Winnik, M. A. *Langmuir* **1994**, *10*, 2495.
(22) White, W. R.; Wiltzius, P. *Phys. Rev. Lett.* **1995**, *75*, 3012.
(23) Wilson, T. In *Confocal Microscopy*; Academic Press: London, 1990.
(24) Jinnai, H.; Yoshida, H.; Kimishima, K.; Funaki, Y.; Ribbe, A.; Hashimoto, T. *Macromolecules*, submitted for publication.
(25) Tanaka, H.; Hayashi, T.; Nishi, T. *J. Appl. Phys.* **1986**, *59*, 3627.
(26) Ribbe, A. E.; Jinnai, H.; Hashimoto, T. *J. Mater. Sci.* **1996**, *31*, 5837.
(27) Jinnai, H.; Nishikawa, N.; Koga, T.; Hashimoto, T. *Macromolecules* **1995**, *28*, 4782.
(28) Jinnai, H.; Koga, T.; Nishikawa, Y.; Hahsimoto, T.; Hyde, S. T. *Phys. Rev. Lett.* **1997**, *78*, 2248.
(29) Jinnai, H.; Hashimoto, T.; Lee, D.; Chen, S.-H. *Macromolecules* **1997**, *30*, 130.
(30) Hashimoto, T.; Jinnai, H.; Nishikawa, Y.; Koga, T.; Takenaka, M. *Prog. Colloid Polym. Sci.* **1997**, *106*, 118.
(31) Hashimoto, T.; Sakamoto, N. *Macromolecules* **1995**, *28*, 4779.
(32) Hashimoto, T.; Sakamoto, N.; Koga, T. *Phys. Rev. E* **1996**, *54*, 5832.
(33) Sakamoto, N.; Hashimoto, T. *Macromolecules* **1998**, *31*, 3815.

MA000752D